ECI Symposium Series, Volume RP5: Proceedings of 7th International Conference on Heat Exchanger Fouling and Cleaning - Challenges and Opportunities, Editors Hans Müller-Steinhagen, M. Reza Malayeri, and A. Paul Watkinson, Engineering Conferences International, Tomar, Portugal, July 1 - 6, 2007

FLUID DYNAMIC GAUGING IN DUCT FLOWS – EXPERIMENTS AND CFD SIMULATIONS

T. Gu, Y.M.J. Chew, W.R. Paterson, D.I. Wilson*

Dept. of Chemical Engineering, University of Cambridge, New Museums Site, Pembroke Street, Cambridge CB2 3RA, UK
*E-mail address: ian_wilson@cheng.cam.ac.uk

ABSTRACT

The technique of fluid dynamic gauging (FDG) has been developed to measure the thickness of deformable foulant deposits on solid immersed in liquid, in real time and *in situ*, with a precision of ± 10 micron. Suction is imposed across a gauging nozzle; the flow rate of liquid through the nozzle allows calculation of the proximity of the nozzle to the surface of the deposit. The technique has been demonstrated by Tuladhar *et al*. (2000) to work well in quasi-static situations, where the bulk liquid is not moving apart from the gauging flow, and in duct flows.

FDG in the quasi-static mode has recently been extended by Chew and co-workers (2004a) using computational fluid dynamics (CFD) simulations of the gauging flow fields to allow the forces imposed on the foulant to be estimated, and thereby test its mechanical strength. We term this technique 'enhanced FDG'.

This paper describes the extension of enhanced FDG to simple duct flows, which requires numerical solution of the governing fluid flow equations in the geometries under consideration. The geometry is that employed by Tuladhar *et al*. (2003), namely a long duct of square cross-section. The experimental results of the present study are compared with the experimental results from Tuladhar *et al.* (2003) and Chew *et al*. (2004b). The CFD results of the study are mainly compared with the present experimental results and with the numerical results from Chew *et al*. (2004a)

INTRODUCTION

Fouling has been a longstanding problem in crude oil refining, and particularly in the operation of exchangers in the distillation preheat train. Fractional distillation uses a substantial proportion of the energy required in oil refining, so the economic and environmental impacts of fouling can be considerable (ESDU, 2000). The growing importance of these impacts led to the start of a major research project on fouling in heat exchangers of crude distillation units in 2006 involving Imperial College London, ESDU, the universities of Bath and Cambridge, and several oil companies. This project will consider crude oil fouling from the molecular to the refinery scale, and represents a significant concerted effort to elucidate the mechanisms of crude fouling and develop the knowledge base to select and specify appropriate mitigation methods.

One activity in the project is the development of a novel test rig employing a tubular annulus section for heat transfer to be constructed at Imperial College London. This device will allow the dynamics of fouling to be studied, and samples of fouling deposits to be recovered for analysis of deposit composition and properties. This test rig will monitor deposit growth via the evolution of pressure drop and thermal resistance. It is proposed that these will be combined with measurements of deposit thickness.

Direct measurement of the thickness of soft foulant layers in a flowing liquid presents a challenge, which has been overcome for several applications by the technique of fluid dynamic gauging (FDG) developed by Tuladhar *et al*. (2000). FDG offers advantages as a fouling thickness sensor, in that (*i*) it is a non-contact technique; (*ii*) measurements are made rapidly *in situ* and in real time; and (*iii*) no knowledge of material parameters is required, except that the foulant layer does not change shape while exposed to the forces imposed by the gauging liquid flow during the measurement. When the gauging flow does cause deformation, the mode and extent of this deformation can be exploited to estimate the strength of the layer by combining the observations with computational fluid dynamics (CFD) simulations of the shear and normal stresses acting on the foulant (Chew *et al*., 2004a).

This paper presents results from experiments (and limited CFD simulations) for an FDG device operating in duct flow in the laminar and transitional flow regimes. CFD is used to calculate the velocity field and hence the stresses imposed on the gauged surface. This represents initial work, in advance of an investigation of dynamic gauging in annular geometries for application in the annulus fouling rig described above. Water is used as the test fluid, both for reasons of safety and because it is a reasonable simulant for crude oil at high temperature and pressure.

PRINCIPLES OF FDG IN DUCT FLOW

Figure 1 illustrates the principles of the dynamic gauging technique. A nozzle of throat diameter d_t is connected to a tube of inner diameter d. The nozzle is fully immersed in a liquid (in this case a filled duct of square cross-section), and positioned close, and normal to, the gauged surface. There are two pressure driving forces operating: (*i*) a fixed hydrostatic suction head, and (*ii*) a pressure head associated with flow in the duct. These

constitute a pressure difference which induces fluid into the nozzle. The discharge liquid is collected and weighed. The discharge mass flow rate m is sensitive to the nozzle clearance ratio h/d_t as shown in Figure 2. The working range of the gauge is in the incremental zone, $h/d_t < 0.25$, where m is usefully responsive to the value of h. Therefore measurement of m may be used to infer h, and subsequently any change in h as a result of deposition or cleaning.

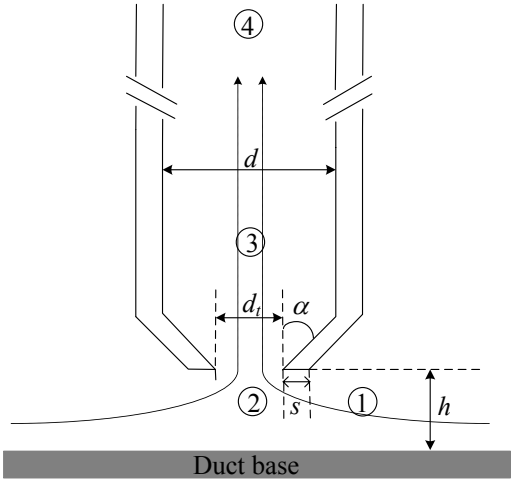

Fig. 1 Schematic of fluid dynamic gauging (FDG).

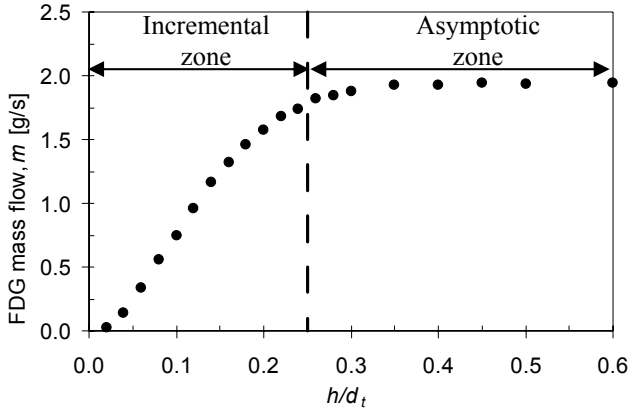

Fig. 2 The working range of FDG for duct flows. The vertical dotted line shows the transition between the zones, operated in nozzle advancing mode for $Re_{duct} = 1390$.

DIMENSIONAL ANALYSIS

The discharge coefficient, C_d, is used to quantify the performance of the nozzle. C_d accounts for the energy losses due to the flow near the nozzle entrance, and is defined as the ratio of the actual to ideal mass flow rate through the nozzle, *viz*.

$$C_d = \frac{m_{actual}}{m_{ideal}} = \frac{m}{\frac{\pi d_t^2}{4}\sqrt{2\rho\Delta p_{13}}} \quad (1)$$

where

$$\Delta p_{13} = \Delta p_{14} - \Delta p_{34} = \rho g H + p_s - \frac{128\mu m l_{eff}}{\pi d^4 \rho} \quad (2)$$

Here, p_s is the static gauge pressure in the duct, H is the hydrostatic head, as shown in Figure 3 (with $H \gg D$), and subscripts 1, 3 and 4 refer to various stations in the tube as shown in Figure 1. l_{eff} is the equivalent length of the tube, allowing for frictional losses caused by the two right-angle bends (Figure 3).

The value of l_{eff} was determined from separate experiments with a reservoir of stagnant liquid, with the nozzle removed from the end of the tube, performed at clearances greater than 20 mm ($h/d_t \gg 2$). The frictional loss Δp_{34} was then balanced by the hydrostatic head $\rho g H$. l_{eff} was found to vary with the tube Reynolds number, and a correlation was obtained for use in Eqn. (2).

EXPERIMENTAL

Figure 3 shows a schematic of the duct flow apparatus. The working fluid was water at 20°C and approximately 1 atm. A gauging nozzle with $d_t = 1$ mm, $d = 4$ mm, $s = 1$ mm and $\alpha = 45°$ was located in a duct of side $D = 15$ mm and length $L = 248$ mm. The duct was constructed from Perspex with a 450 mm (30D) entry section to ensure fully developed flow. The mean velocity through the duct was in the range 0.0077 - 0.74 m/s (Re_{duct} 116 – 11 100). The gauge was positioned with its centre-line on the central vertical plane of the duct, 70 mm from the entrance. The clearance between the gauging surface at the base of the duct and the nozzle was adjusted by a micrometer (resolution ± 2 μm). The nozzle approaches the gauging surface in advancing mode, *i.e.* starting from $h/d_t \geq 1$. The discharge gauging flow was collected using an electronic balance (accuracy ± 0.05g).

The gauge was connected to a siphon tube of length $l = 640$ mm open to the atmosphere with $H = 307$ mm. This fixed hydrostatic head provides the principal driving force for the gauging flow. The second driving force originates from the static gauge pressure in the duct, associated with the bulk flow. This duct static pressure was measured near the inlet using a pressure sensor (accuracy ± 34 Pa). The static gauge pressures ranged from 388 Pa ($Re_{duct} = 116$) to 17 200 Pa ($Re_{duct} = 11\,000$).

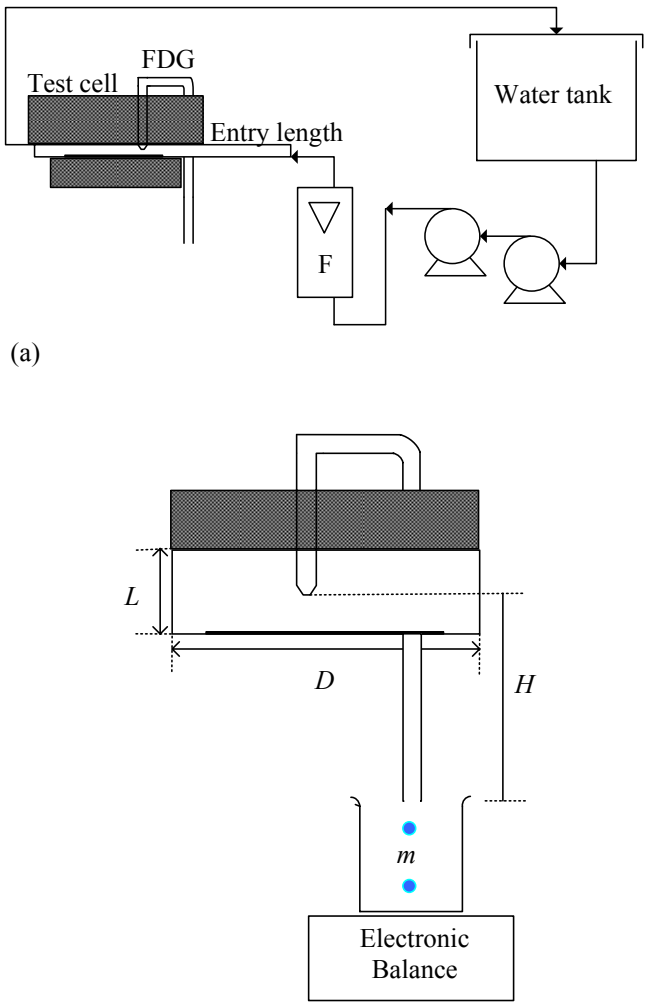

Fig. 3 Schematic of duct flow apparatus.
(a) flow loop, (b) test section.

EXPERIMENTAL RESULTS AND DISCUSSION

Figure 4 shows data plotted against the nozzle clearance ratio for duct Reynolds number ranging from 440 to 2220 at constant H (307 mm). Data reported by Tuladhar *et al.* (2003) are also plotted. The data are plotted in the form of the normalised FDG discharge flow, m^*, defined as the mass flow rate, m, divided by the asymptotic discharge mass flow rate, m_∞ (obtained at large h/d_t). The two sets of results show good agreement. The profiles display the same feature: a steep, incremental region at small h/d_t and an asymptotic region at larger h/d_t, where the gauging flow was independent of clearance. The transition between these two regions lay at $h/d_t = 0.25$ approximately, in agreement with the values reported by Tuladhar *et al.* (2003). It is evident from Figure 4 that there was a small shift in the data points at lower clearances, $h/d_t < 0.3$, caused by new micrometer fittings. Nonetheless, the practical working range for the gauge was still in the region $0.05 < h/d_t < 0.25$.

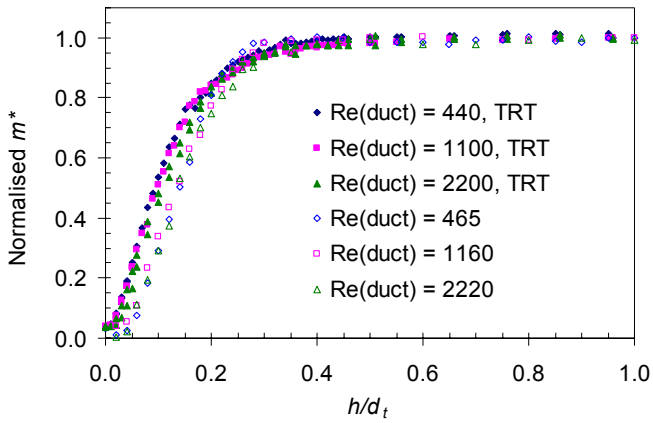

Fig. 4 Comparison of normalised FDG discharge mass profiles for laminar duct flow. Solid symbols (TRT) - data from Tuladhar *et al.* (2003): open symbols – this work.

Figure 5 shows the gauging profiles obtained for increasing Re_{duct}; the working range is wider as Re_{duct} increases: for $Re_{duct} > 10\,000$ the nozzle can usefully be as far as $h/d_t = 0.4$ from the base. Since the hydrostatic head was fixed, m_∞ varied with duct static pressure. The effect of flow rate on static pressure and asymptotic gauge discharge flow is presented in Figure 6.

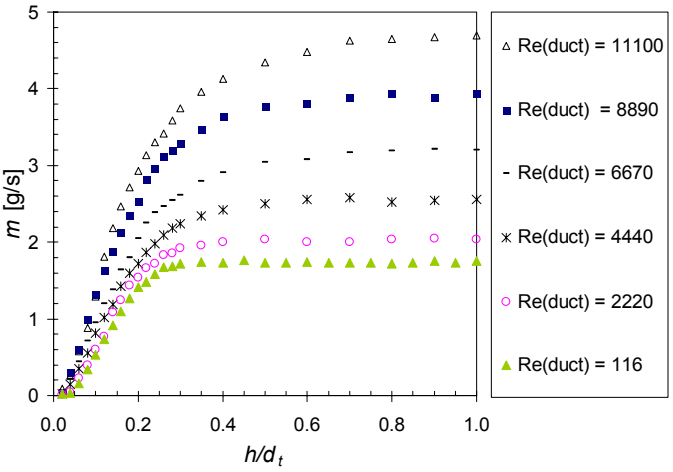

Fig. 5 Effect of Re_{duct} on FDG discharge profiles.

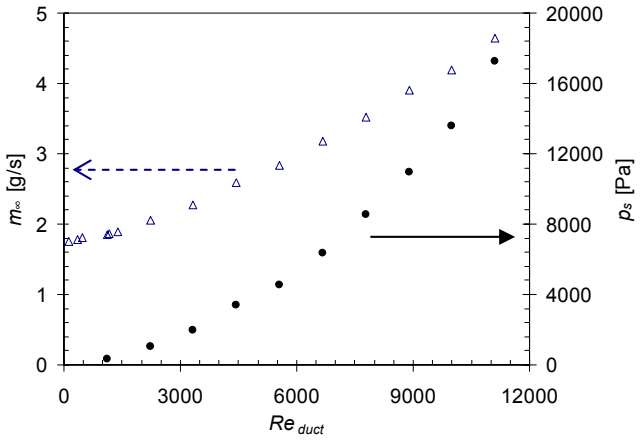

Fig. 6 Effect of Re_{duct} on static gauge pressure (dots) and asymptotic discharge flow rate (triangles).

The data from Figure 5 are re-plotted in terms of the discharge coefficient in Figure 7, alongside data reported for quasi-stagnant flow conditions using a similar nozzle and fixed hydrostatic head H = 330 mm *cf*. H = 307 mm (this work). All profiles exhibit an increase towards an asymptotic value of C_d, termed $C_{d,\infty}$, reached around h/d_t = 0.5. The differences in the transition from the incremental to the asymptotic zone, which are quite noticeable in Figure 5, are much less apparent in this representation and indicate that the difference in mass flow rates is related to the variation of l_{eff} with Re_{duct}. The C_d profiles for the quasi-stagnant mode are very similar to the duct flow experiments, confirming the observations of Tuladhar *et al*. (2003).

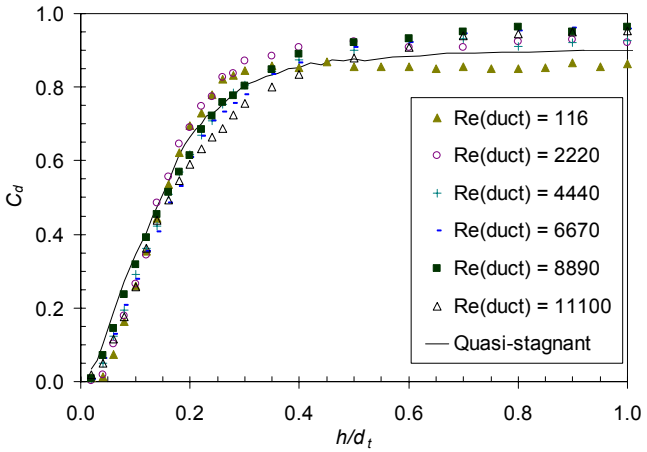

Fig. 7 C_d versus h/d_t. Points – data, this work. Line – quasi-stagnant gauging, reported by Chew *et al*. (2004b) using water at 20°C.

Some differentiation is evident when the asymptotic discharge coefficient $C_{d,\infty}$ is considered (Figure 8). The $C_{d,\infty}$ values observed in the laminar regime are slightly smaller than that obtained in the quasi-stagnant case. $C_{d,\infty}$ increases with Re_{duct} and becomes relatively stable in the transitional/ turbulent region (Re_{duct} > 6000) approaching a value of 0.96. This variation, although small, suggests that there is some mild degree of interaction between the gauging flow and the duct flow.

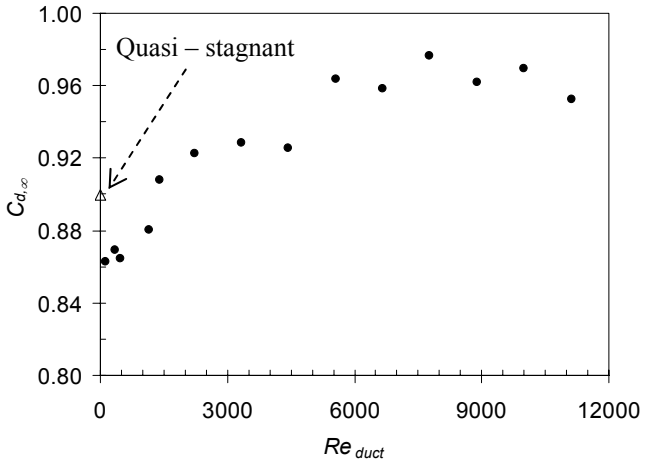

Fig. 8 Variation of $C_{d,\infty}$ with Re_{duct} in the asymptotic zone (h/d_t = 1.5). Triangle shows quasi-stagnant result from Chew *et al*. (2004b).

As FDG withdraws fluid from the duct, it is important to establish the fraction of flow diverted through the gauge. Figure 9 plots the ratio of the asymptotic flow through the gauge to that in the duct inflow, m_∞ / m_{duct}, for the cases considered above. Both increase with Re_{duct} and it is evident that below Re_{duct} = 465, a significant proportion of the liquid in the duct inflow is withdrawn into the gauge (≥ 30%), whereas for Re_{duct} > 1390, less than 10% of the bulk inflow is withdrawn through the gauge. It is postulated that this could be a contributing factor to the deviation in $C_{d,\infty}$ evident in Figure 8.

Furthermore, this factor must be considered in designing a gauge for monitoring studies: clearly, the measurement device (FDG) should be sized as not to substantially reduce the flow downstream of the sensor, as illustrated in Figure 9 for Re_{duct} = 116. In this case, virtually all the duct inflow is withdrawn into the gauge. This is undesirable as the aim of the gauge is to bleed, not to bypass the main flow in the duct. For the duct apparatus, there is therefore a threshold of operation. It is desirable to operate the gauge above Re_{duct} = 1000, where less than 10% of the liquid in the duct inflow is bled via the gauge.

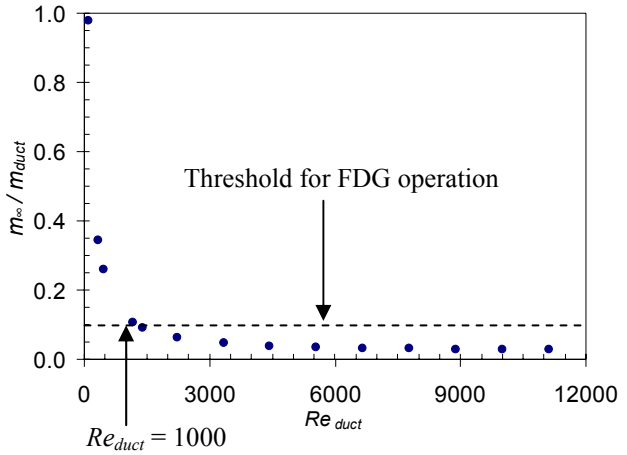

Fig. 9 Fraction of mass flow withdrawn through the gauge. Operating conditions as in Fig. 5

It is also useful to consider the interaction between the gauging nozzle and the slower moving fluid near the wall as the flow becomes less laminar and develops turbulent characteristics. Figure 10 shows the variation of the thickness of the viscous sub-layer with Re_{duct}.

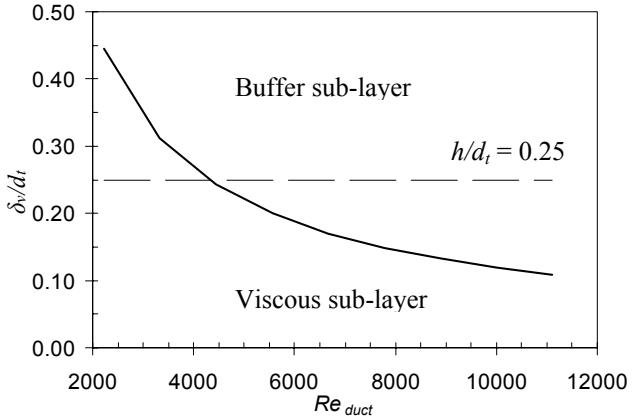

Fig. 10 Estimated viscous sub-layer thickness ratio.

The thickness of the viscous sub-layer, δ_v, and buffer sub-layer were estimated using the universal velocity profile $y^+ = 5$ (Kay and Nedderman, 1979), where y^+ is given by

$$y^+ = \frac{\delta \rho u_m}{\mu}\sqrt{C_f/2}$$

and C_f was estimated using the Blasius correlation, $C_f = 0.079 Re_{duct}^{-0.25}$ (Kay and Nedderman, 1979). The Blasius correlation is valid for Reynolds number 4000 to 10 000. The accuracy of this analysis is weaker in the transitional regime, particularly below $Re_{duct} < 4000$.

Figure 10 shows that δ_v/d_t decreases from 0.445 at Re_{duct} = 2220 to 0.109 at Re_{duct} = 11 100, (albeit neglecting the effect of the gauging nozzle protruding into the flow field). The figure shows that below Re_{duct} = 4500, the tip of the nozzle was submerged in the region notionally occupied by the viscous sub-layer: the validity of this interpretation is somewhat tenuous given that this Reynolds number is associated with the transitional flow regime, when the universal velocity profile is unlikely to be an accurate description of the flow. Nevertheless, the figure does indicate that the extended sensitivity of the gauging regime (incremental behaviour observed at larger values of h/d_t) is associated with the nozzle operating in the buffer sub-layer.

CFD MODEL OF FDG IN DUCT FLOW

CFD simulations of the gauging configuration in laminar flow were done add to the experimental findings, for the prediction of the normal and shear stresses acting on the surface being gauged. The incompressible Navier-Stokes equations are solved using the finite element method (FEM) software COMSOL MULTIPHYSICS™ version 3.3, Chemical Engineering Module on a 2.41 GHz processor PC with 3.00 GB RAM. The calculations employ the steady-state, stationary Lagrangian mode. The vector notations of the continuity and the steady-state, incompressible Navier-Stokes equations are:

Continuity: $$\nabla \cdot \vec{\boldsymbol{v}} = 0 \qquad (3)$$

Navier-Stokes: $$\rho \vec{\boldsymbol{v}} \cdot \nabla \vec{\boldsymbol{v}} = -\nabla p + \mu \nabla^2 \vec{\boldsymbol{v}} + \rho g \qquad (4)$$

where $\vec{\boldsymbol{v}}$ is velocity vector, p is pressure, ρ is the density and g is acceleration due to gravity, set to zero in this case for computational convenience.

Model set-up

The geometry was half of the duct exploiting symmetry (Figure 11). The field includes a suction tube positioned with its axis perpendicular to the longitudinal axis of the duct. Note that for computational convenience, the tube is straight, so that H in Figure 3 (b) has no meaning in the simulation. The aspect ratios are L/D = 11 and l/d = 16.5. The fluid flows into the duct and a fraction discharges through the gauging tube. The remaining fluid leaves the duct at the outlet.

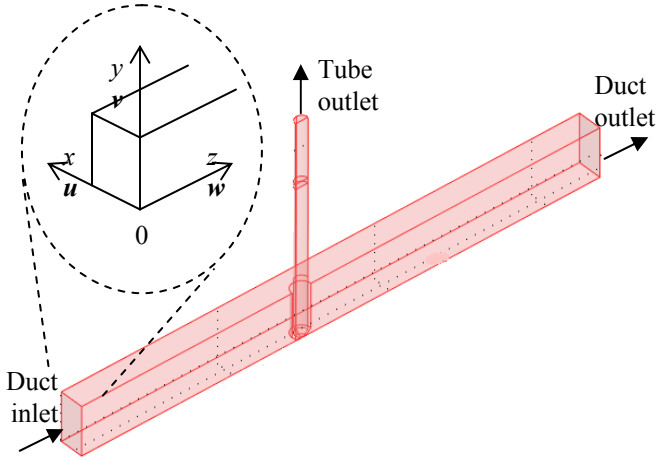

Fig. 11 Model of the flow system. Velocity vector in *y*-direction denoted $\boldsymbol{v}$, in *z*-direction, $\boldsymbol{w}$, and in *x*-direction, $\boldsymbol{u}$.

The inputs to the model are the velocity at the duct inlet and tube outlet, and pressure at the duct outlet, all of which have been extracted from the experimental data. The output of the model is the pressure at the tube outlet. The pressure difference between tube outlet and test section outlet is Δp_{13}. An overview of the boundaries is given in Table 1.

Table 1 Overview of model input and output.

Boundary	Input	Output
Duct inlet	*z*-wise velocity	pressure
Duct outlet	pressure	velocity
Tube outlet	*y*-wise velocity	pressure

BOUNDARY CONDITIONS

Duct inlet

At the duct inlet, fully developed flow was assumed, so that the *z*-wise velocity is approximately by Eqn. (5) (COMSOL MULTIPHYSICS™, ChemEng Model Library)

$$\boldsymbol{w} = \frac{16 \times w_{\max} \{(x+0.5D)(D-(x+0.5D))\} \times \{y(D-y)\}}{D^4} \quad (5)$$

where x and y are the width-wise and height-wise coordinates of the duct inlet plane. $\boldsymbol{w}_{max}$ is the maximum *z*-wise velocity, being approximately twice the mean *z*-wise velocity: $\boldsymbol{w}_{\max} = 2 \times \boldsymbol{w}_{mean}$. The value of $\boldsymbol{w}_{mean}$ was taken from the experimental data.

The *x*-wise and *y*-wise velocities $\boldsymbol{u}$ and $\boldsymbol{v}$ are zero at the duct inlet.

$$\boldsymbol{u} = \boldsymbol{v} = 0$$

Tube outlet

Experimental data indicate that the flow in the gauging tube was in the laminar regime. Therefore, fully developed flow was assumed, given by

$$\boldsymbol{v} = \boldsymbol{v}_{max}\left(1 - \left(\frac{r}{R}\right)^2\right) \quad (6)$$

where r is the radial coordinate measured from the tube centre-line, R is the inner radius of tube, and $\boldsymbol{v}_{max}$ is the *y*-wise velocity on the tube centre-line, expressed as twice the mean velocity as calculated from experimental data.

The *x*-wise and *z*-wise velocities $\boldsymbol{u}$ and $\boldsymbol{w}$ are zero at the tube outlet.

$$\boldsymbol{u} = \boldsymbol{w} = 0$$

Duct outlet

The boundary condition at the outlet of the duct was:

$$\boldsymbol{u} = \boldsymbol{v} = 0$$
$$p = -414\ Pa$$

where $\boldsymbol{u}$ and $\boldsymbol{v}$ are the *x*-wise and *y*-wise velocities and p the outlet pressure, a value taken from the experimental data. The negative sign is used to impose flow into the gauge.

Walls

At walls both the tangential and normal components of the velocity equal to zero, *i.e.* the wall is impermeable. The no-slip condition is applied to all wall boundaries in the system, including the walls of the duct and the inner and outer walls of the gauge.

Symmetry

Along the *y*-*z* plane of symmetry the normal components of the velocity is zero.

Mesh

A *fine* mesh was selected from the predefined mesh settings. This automatically determines the maximum scaling factor (0.8), element growth rate (1.45), mesh curvature factor (0.5) and cut-off (0.02) as well as resolution of narrow regions (0.6). A higher concentration of mesh/grid elements was assigned to the clearance region beneath the nozzle, where the velocity gradients are largest. At the nozzle rim the mesh element growth rate was set to 1. The element growth rate determines the maximum rate at which the element size can grow from a region of small elements to a region of larger elements. Setting the element growth rate to 1, means that the spatial element size can grow by 0% from one element to the next in the nozzle clearance region. In essence this ensures that flow resolves satisfactorily in the critical gap between the nozzle and the surface. Figure 12 shows the region of highest mesh density. Mesh statistics were: number of degrees of freedom, 110 029; number of elements, 20 415; and minimum element quality, 0.1497.

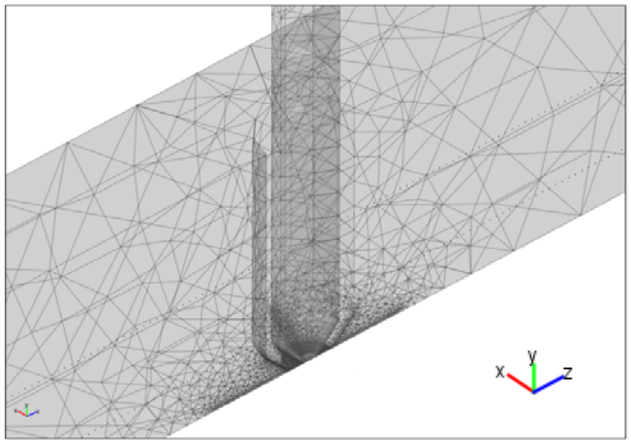

Fig. 12 FEM mesh in the nozzle region.

CFD RESULTS

In the experiment the mass flow rate is an output parameter which determines the thickness. In the numerical model the mass flow rate is explicitly prescribed via $\boldsymbol{v}_{\max}$. The output from the numerical model is the pressure drop Δp_{13}, which is used to calculate C_d via Eqn. (1).

The results from a converged run are presented. The solution took 148 minutes to converge. Figure 13 illustrates the z-wise velocity for the case where h/d_t = 0.06, Re_{duct} = 116 ($\boldsymbol{w}_{\max}$ = 0.0155 m/s) and Re_{tube}= 49. The physical properties were those of water at 20ºC. Upstream of the gauge the highest z-wise velocity was found on the duct centre-line, as expected for the case of a fully developed duct inlet velocity. The z-wise velocity shows an acceleration in the region between the tube and the vertical wall of the duct, and a re-circulation region appears immediately downstream of the tube in its wake.

From the experiment Δp_{13} is found via Equation (2). In the simulation Δp_{13} is found by adding the pressure head with the tube outlet pressure. The calculated pressure at the duct inlet was -413.8 Pa, which was very close to the outlet value (-414 Pa). At the tube outlet the pressure was -2771 Pa. Therefore the pressure difference between the duct inlet and the gauge outlet was -3185 Pa (-2771 Pa + -413.8 Pa) which yields a C_d value of 0.0725 using Equation (1). The experimental value is 0.073; the difference, at < 1%, is deemed to be acceptable.

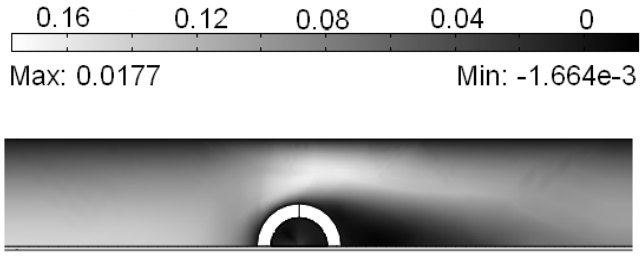

Fig. 13 Distribution of z-wise velocity on the x-z plane at $y = 0.5D$ for laminar flow in the duct Re_{duct} = 116, Re_{tube} = 49, and h/d_t = 0.06.

Figure 14 shows the y-wise velocity in the tube. Clearly, the flow in the tube was not symmetric in the y-z plane of geometric symmetry until some distance upwards from the nozzle throat due to the influence of the duct flow.

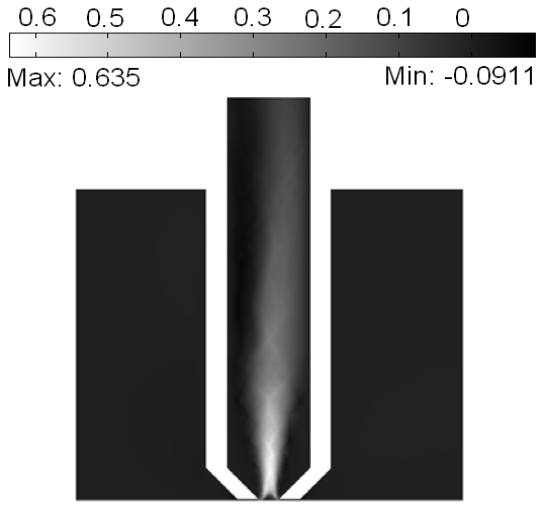

Fig. 14 y-wise velocity in the tube in the y-z plane of symmetry.

The streamlines near the nozzle suction region are plotted in Figure 15. The flow was mainly *z*-wise in the duct but when approaching the nozzle the flow develops a *y*-wise component (Fig. 15 (a)). Divergent flow is evident in the nozzle expansion, with no recirculation evident further up the tube under this combination of Re_{duct}, Re_{tube}, h/d_t, s and l/d. Chew *et al*. (2004a) simulated laminar gauging flows in a similar nozzle geometry with a quasi-stagnant fluid and showed that the flow patterns within the tube were sensitive to Re_{tube}, h/d_t and s. Further simulation is required to test whether these parameters have a significant effect on the flow pattern in the tube when the flow in the duct is faster.

Recirculation downstream of the gauge is evident from the swirling streamlines in Figure 15 (a) and is caused by the obstruction of the gauge when the duct flow passes it. Figure 15 (b) shows the streamlines projected on the *x*-*z* plane, indicating fluid being withdrawn into the nozzle.

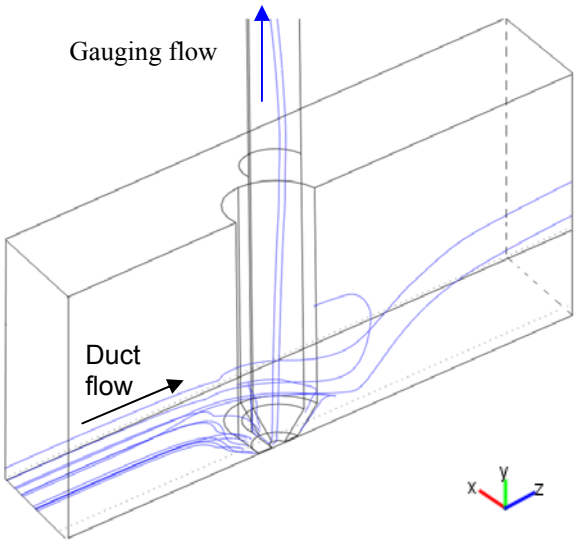

(a)

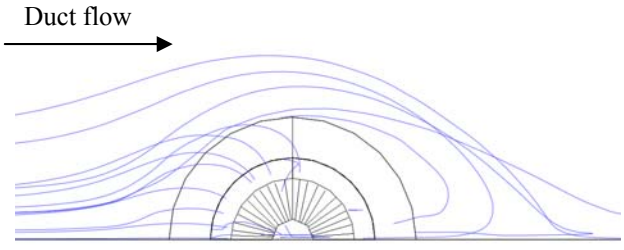

(b)

Fig. 15 Samples of fluid flow patterns near the nozzle suction region for Re_{duct} = 116, Re_{tube} = 49, and h/d_t = 0.06: (a) streamlines; (b) streamline projected onto the *x*-*z* plane.

Figure 16 shows the distribution of normal stress, τ_{yy}, acting on the base of the duct for h/d_t = 0.06, Re_{duct} = 116 and Re_{tube} = 49. Consider the geometry of the nozzle rim projected onto the duct base. The plot shows that the peak normal stress (approximately -25 Pa) was located beneath the inner rim of the nozzle and that the normal stress distribution was approximately symmetrical about the centre-line of the tube. The simulation results are consistent with experimental observations in duct flow reported by Tuladhar (2001); he recorded that his deposit distortion was most often located beneath the rim of the nozzle, due to normal stress caused by the gauging flow.

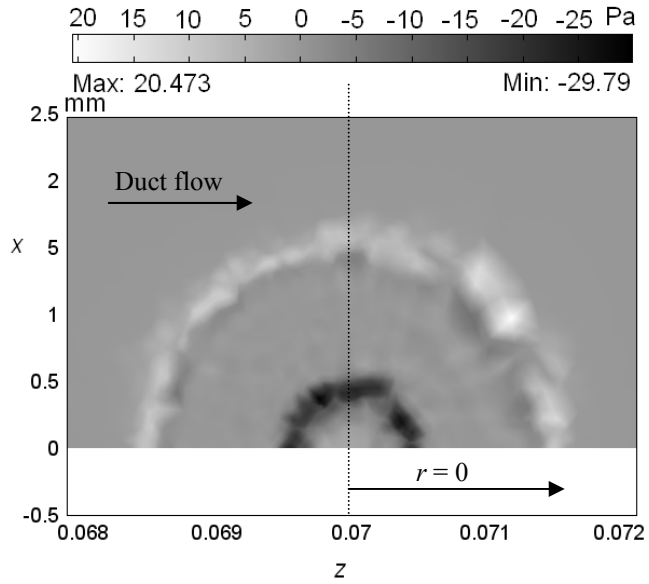

Fig. 16 Normal stress (τ_{yy}) distribution on the duct base beneath the gauge for Re_{duct} = 116, Re_{tube} = 49, and h/d_t = 0.06.

Figure 17 compares the *z*-wise shear stress distribution with that calculated for the quasi-stagnant system by Chew *et al*. (2004a). Both distributions are reasonably symmetrical and under these conditions the two simulations show very good agreement. The *z*-wise shear stress again showed a maximum at r = 0.5 mm, beneath the inner radius of the nozzle, and a small peak beneath the outer radius, r = 1.5 mm.

The magnitude of the *z*-wise shear stress was of the order of (±) 70 Pa, and was effectively independent of the tube length to diameter ratio (l/d) for the same Re_{duct} = 116. This can be compared with the shear stress created by the duct flow alone, of the order of 0.001 Pa: this result indicates that the shear stress acting on the base of the duct underneath the gauging nozzle is dominated by the suction flow. There is

therefore an opportunity to revisit Tuladhar's data (2001) on the cleaning of whey protein concentrate foulants, particularly for those cases where he noted that the gauge flow appeared to disrupt his swollen foulant layer.

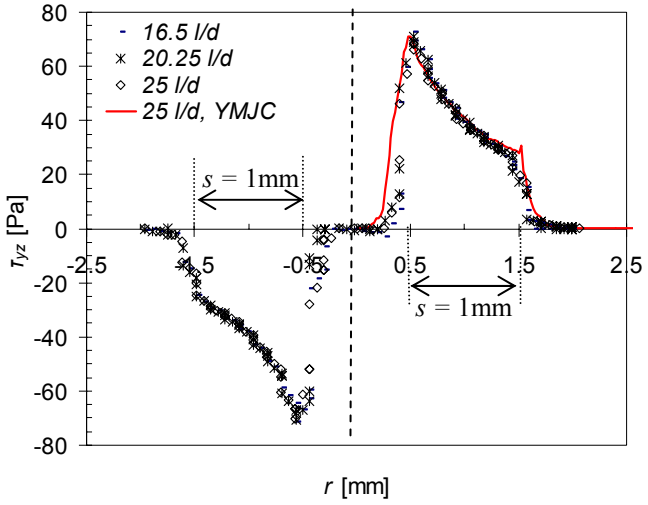

Fig. 17 Comparison of shear stress distributions on the base directly beneath the gauge for $Re_{duct} = 116$, $Re_{tube} = 49$, $h/d_t = 0.06$ and $s = 1$ mm. Line shows quasi-stagnant simulation from Chew *et al*. (2004a).

CONCLUSIONS

This study demonstrates that fluid dynamic gauging can be applied to duct flows and shows good agreement with the previous results of Tuladhar (2003). The fraction of the duct flow which leaves through the gauge was highest for laminar duct flow.

For the first time, CFD has been successfully applied to simulate FDG in a duct flow system for steady, incompressible, laminar flows. Experimental data and simulation results agree to within 1% for the current model, supporting the validity of both the experiments and the assumptions underpinning the simulation.

ACKNOWLEDGEMENTS

Software training from Basil Lam (Dept. of Chemical Engineering, Cambridge University, UK) is gratefully acknowledged, as is financial support from the Engineering and Physical Sciences Research Council (EPSRC EP/D50306X) and experimental data from T.R. Tuladhar and R. J. Hooper.

NOMENCLATURE

C_d	discharge coefficient accounting for nozzle flow complexity and energy loss, dimensionless
C_f	Blasius friction factor, dimensionless
d	inner diameter of tube, m
D	duct side, m
g	acceleration due to gravitaty, m/s^2
h	clearance between nozzle tip and gauging surface, m
H	hydrostatic head providing pressure driving force for gauging flow, m
s	width of nozzle rim, m
L	duct length, m
l	length of siphon tube, m
m	tube discharge mass flow rate, kg/s
p	pressure, Pa
r	radial coordinate of the siphon tube, m
R	inner radius of the siphon tube, m
Re	Reynolds number, dimensionless
u	x-wise velocity, m/s
v	y-wise velocity, m/s
w	z-wise velocity, m/s
y^+	dimensionless thickness ratio, m

Greek

α	nozzle inner angle, °
δ	sub-layer, m
ρ	density, kg/m^3
μ	dynamic viscosity, Pa.s

Subscripts

*	normalised
s	static
t	throat
v	viscous
∞	asymptotic
duct	duct
eff	effective
max	maximum

ABBREVIATIONS

CFD	computational fluid dynamics
FDG	fluid dynamic gauging
FEM	finite element method

REFERENCES

J.Y.M. Chew, S.S.S. Cardoso, W.R. Paterson, D.I. Wilson, 2004a, CFD studies of dynamic gauging, *Chemical Engineering Science,* Vol. 59, pp. 3381-3398.

J.Y.M. Chew, W.R. Paterson, D.I. Wilson, 2004b, Fluid dynamic gauging for measuring the strength of soft deposits, *Journal of Food Engineering,* Vol. 65, pp. 175-187.

T.R. Tuladhar, W.R. Paterson, D.I. Wilson, 2003, Dynamic gauging in duct flows, *The Canadian Journal of Chemical Engineering*, Vol. 81, pp. 279-284

T.R. Tuladhar, W.R. Paterson, D.I. Wilson, N. Macleod, 2000, Development of a novel non-contact proximity gauge for thickness measurement of soft deposits and its application in fouling studies, *The Canadian Journal of Chemical Engineering*, Vol. 78, pp. 925-947

T.R. Tuladhar, 2001, Development of a novel sensor for cleaning studies, PhD dissertation, University of Cambridge, UK

J.M. Kay and R.M. Nedderman, 1979, *An introduction to fluid mechanics and heat transfer* 3rd edn., chapter 14, pp. 186, 187, Cambridge University Press, UK

ESDU (Engineering Sciences Data Unit), 2000, Heat exchanger fouling in the preheat train of crude oil distillation levels, *Data Item 0016*, ESDU Intl., London, UK.

COMSOL MULTIPHYSICS™ version 3.3, Chemical Engineering Module, 2006, Chemical Engineering Model Library, Porous Reactor with Injection Needle